

5-13-2020

## Mesopause Airglow Disturbances Driven by Nonlinear Infrasonic Acoustic Waves Generated by Large Earthquakes

P. A. Inchin

*Embry-Riddle Aeronautical University, INCHINP@my.erau.edu*

J. B. Snively

*Embry-Riddle Aeronautical University, snivelyj@erau.edu*

J. Aguilar Guerrero

*Embry-Riddle Aeronautical University, aguila9@my.erau.edu*

M. D. Zettergren

*Embry-Riddle Aeronautical University, zettergm@erau.edu*

A. Williamson

*University of Oregon*

*See next page for additional authors*

Follow this and additional works at: <https://commons.erau.edu/publication>



Part of the [Geophysics and Seismology Commons](#)

---

### Scholarly Commons Citation

Inchin, P. A., Snively, J. B., Williamson, A., Melgar, D., Aguilar Guerrero, J., & Zettergren, M. D. (2020). Mesopause airglow disturbances driven by nonlinear infrasonic acoustic waves generated by large earthquakes. *Journal of Geophysical Research: Space Physics*, 125, e2019JA027628. [https:// doi.org/ 10.1029/2019JA027628](https://doi.org/10.1029/2019JA027628)

This Article is brought to you for free and open access by Scholarly Commons. It has been accepted for inclusion in Publications by an authorized administrator of Scholarly Commons. For more information, please contact [commons@erau.edu](mailto:commons@erau.edu).

---

**Authors**

P. A. Inchin, J. B. Snively, J. Aguilar Guerrero, M. D. Zettergren, A. Williamson, and D. Melgar

# JGR Space Physics

## RESEARCH ARTICLE

10.1029/2019JA027628

### Key Points:

- Mesopause airglow responses to infrasonic acoustic waves generated by near-epicentral seismic motions are investigated numerically in 3D
- Large earthquakes can drive substantial and detectable perturbations in mesopause airglow via acoustic waves
- Airglow observations may help to investigate earthquake dynamics and supplement tsunami early-warning systems

### Supporting Information:

- Supporting Information S1
- Figure S1
- Figure S2
- Movie S1
- Movie S2

### Correspondence to:

P. A. Inchin,  
 inchinp@erau.edu

### Citation:






Inchin, P. A., Snively, J. B., Williamson, A., Melgar, D., Aguilar Guerrero, J., & Zettergren, M. D. (2020). Mesopause airglow disturbances driven by nonlinear infrasonic acoustic waves generated by large earthquakes. *Journal of Geophysical Research: Space Physics*, 125, e2019JA027628. <https://doi.org/10.1029/2019JA027628>

Received 14 NOV 2019

Accepted 21 APR 2020

Accepted article online 13 MAY 2020

## Mesopause Airglow Disturbances Driven by Nonlinear Infrasonic Acoustic Waves Generated by Large Earthquakes

P. A. Inchin<sup>1</sup> , J. B. Snively<sup>1</sup> , A. Williamson<sup>2</sup> , D. Melgar<sup>2</sup> , J. Aguilar Guerrero<sup>1</sup> , and M. D. Zettergren<sup>1</sup> 

<sup>1</sup>Department of Physical Sciences and Center for Space and Atmospheric Research, Embry-Riddle Aeronautical University, Daytona Beach, FL, USA, <sup>2</sup>Department of Earth Sciences, University of Oregon, Eugene, OR, USA

**Abstract** Near-epicentral mesopause airglow perturbations, driven by infrasonic acoustic waves (AWs) during a nighttime analog of the 2011 M9.1 Tohoku-Oki earthquake, are simulated through the direct numerical computation of the 3D nonlinear Navier-Stokes equations. Surface dynamics from a forward seismic wave propagation simulation, initialized with a kinematic slip model and performed with the SPEC3D\_GLOBE model, are used to excite AWs into the atmosphere from ground level. Simulated mesopause airglow perturbations include steep oscillations and persistent nonlinear depletions up to 50% and 70% from the background state, respectively, for the hydroxyl OH(3,1) and oxygen O(<sup>1</sup>S) 557.7-nm emissions. Results suggest that AWs excited near a large earthquake's epicenter may be strong enough to drive fluctuations in mesopause airglow, some which may persist after the AWs have passed, that could be readily detectable with ground- and/or satellite-based imagers. Synthetic data demonstrate that future airglow observations may be used for the characterization of earthquake mechanisms and surface seismic waves propagation, potentially complementing tsunami early-warning systems based on total electron content (TEC) observations.

**Plain Language Summary** Large earthquakes can produce substantial Earth's surface deformation. For earthquakes that occur offshore, sea floor deformation may also result in ocean surface displacements that generate tsunamis. At the interface with the atmosphere, these displacements can serve as a source of very low frequency acoustic waves. Reaching the upper atmosphere (~70 km and higher), these waves can be strong enough to form shock waves and generate observable disturbances. This paper reports the results of numerical simulations of ~80–90-km altitude airglow disturbances driven by strong acoustic waves excited during a hypothetical nighttime equivalent of the 2011 Tohoku-Oki earthquake (magnitude 9.1). Modeling results show that, for such large earthquakes if occurring at nighttime, airglow disturbances could be readily detected with specialized ground- and space-based imagers. The possibility to detect airglow disturbances earlier than the arrival of the tsunami at the shore points to the potential applicability of such observations for tsunami early-warning systems. Also, the results suggest that such observations can be a useful tool for the characterization of earthquake processes and the propagation of seismic waves.

## 1. Introduction

Seismically-induced acoustic and gravity waves (AWs or, collectively, AGWs) that reach ionospheric heights can trigger detectable plasma perturbations (e.g., Bolt, 1964; Jin et al., 2015). For the investigation of these perturbations, total electron content (TEC) measurements are the most common and accurate source of data presently used (Komjathy et al., 2016). However, TEC detects ionospheric electron density fluctuations mostly from the bottom side of the F-layer (~250–300 km), where the coupling of neutral gas with plasma is significant, but where neutral waves are also strongly dissipated by viscosity. The observations of near-infrared hydroxyl OH(3,1) with its band center at ~1,504.7-nm and oxygen O(<sup>1</sup>S) 557.7-nm airglow emissions, at altitudes ~85–95 km, may supplement the study of natural hazard-driven AGWs (Pilger et al., 2013), providing more timely measurements than TEC in a less dissipative region of the atmosphere (Blanc, 1985). Pilger and Bittner (2009) numerically investigated possible mesopause airglow (MA) perturbations of AWs from tropospheric sources. Bittner et al. (2010) reported mesopause temperature perturbations up to ~5 K from tsunami-excited

AGWs. Snively (2013) reported simulation results of airglow perturbations of AGWs from tropospheric forcing by convection. Here, we report the results of the simulation of MA perturbations generated by AWs during a large earthquake at the region near its epicenter, where amplitudes may be sufficient to impose lasting and detectable nonlinear impacts.

The 2011 M9.1 Tohoku-Oki earthquake in Japan occurred at 14:46 LT (JST) 11 March 2011 and was one of the largest recent megathrust earthquakes, causing a devastating tsunami. The hypocenter was located at  $\sim 70$  km off the coast of Japan ( $38.103^\circ\text{N}$ ,  $142.861^\circ\text{E}$ ) at the depth of  $\sim 24$  km (Japan Meteorological Agency, JMA). An unprecedented amount of TEC data were collected during the earthquake and tsunami in Japan (Galvan et al., 2012; Tsugawa et al., 2011) and, for example, on the Hawaiian islands (Makela et al., 2011) and the continental part of the United States (Azeem et al., 2017). Important aspects of AGW dynamics and coseismic ionospheric disturbances were described, including seismic wave-driven AW perturbations in the ionospheric plasma, acoustic resonances, and plasma depletion (Liu et al., 2011; Maruyama & Shinagawa, 2014; Saito et al., 2011). Yang et al. (2017) observed tsunami-induced airglow emission perturbations retrieved from the Sounding of the Atmosphere using Broad-band Emission Radiometry (SABER) instrument onboard the Thermosphere-Ionosphere-Mesosphere Energetics Dynamics (TIMED) spacecraft. Coisson et al. (2015) reported tsunami-induced TEC perturbations using satellite radio occultation data. Makela et al. (2011) reported observations and simulation of 630.0-nm ionospheric airglow emission perturbations, driven by the tsunami over the Hawaiian Islands. And, Smith et al. (2015) reported observations of 630.0-nm ionospheric and 557.7-nm mesopause airglow emission perturbations extending over Argentina.

Numerous studies were dedicated to earthquake/tsunami-atmosphere-ionosphere coupling process modeling for this event. Recent investigations have confirmed the nonlinear AWs above the source in detail. Among them, Shinagawa et al. (2013) reported simulation results of driven plasma disturbances using nonlinear compressible fluid equations based on a neutral gas model coupled with a single-fluid collisional plasma model in 2D. Matsumura et al. (2011) simulated near-field AGW dynamics based on a 2D nonlinear compressible neutral gas model. Zettergren et al. (2017) presented modeling results of ionospheric responses to a ground-level axisymmetric source of AGWs in a 2D nonlinear atmosphere model, and electron density depletions (“ionospheric hole” formation) in TEC signatures were simulated with a 2D multifluid plasma model. Meng et al. (2018) simulated ionospheric responses in 3D, using a point source representation of excited AGWs at ground level and assuming a linear regime of their propagation at altitudes lower than  $\sim 100$  km. Zettergren and Snively (2019) simulated AGWs and plasma perturbations using a 3D multifluid ionosphere model coupled with a 2D axisymmetric nonlinear compressible atmospheric model and investigated the latitudinal asymmetry of plasma responses, dynamics of driven electric currents, and geomagnetic field perturbations. These studies point to the excitation of strong near-epicentral AGWs, causing substantial ionospheric responses, in agreement with TEC observations. However, in these studies, ground-level AGW sources are highly simplified, omitting time and spatial dynamics of the rupture, which extended for hundreds of kilometers and lasted more than a minute (Satake et al., 2013). In addition to simplified modeling assumptions, this may result in marked inconsistency with real coupling mechanisms and preclude comparisons of the resulting AW fields with higher-resolution data than TEC, such as MA imagery.

Here, realistic surface displacements, driven by a model description of the 2011 Tohoku-Oki earthquake, are used to excite AWs at the ground-level boundary of the 3D neutral atmosphere Model for Acoustic-Gravity wave Interactions and Coupling (MAGIC) (Snively, 2013). Whereas the previously mentioned studies focused on ionospheric responses, the aim of the present study is to investigate and demonstrate the possibility to detect perturbations in MA, triggered by AWs at the region near the epicenter. We also constrain wave field amplitudes, in comparison to prior simulations by Zettergren et al. (2017) and Zettergren and Snively (2019). Although the earthquake happened during the day and MA observations are most feasible at nighttime, the amplitudes of simulated AW perturbations in the daytime background atmosphere are similar to those in a nighttime atmosphere, so they can be readily compared. This case study thus demonstrates the hypothetical observability of a Tohoku-Oki-like earthquake under nighttime airglow chemistry assumptions, for the hydroxyl OH(3,1) band and OI 557.7-nm green line emission. Our results suggest that, although they may be limited to nighttime scenarios, MA observations can be a valuable source of information on coseismic AWs, in particular for large earthquakes. They can provide an additional high-resolution data source for seismological studies and enable the detection of waves minutes prior to their arrival in the ionosphere.

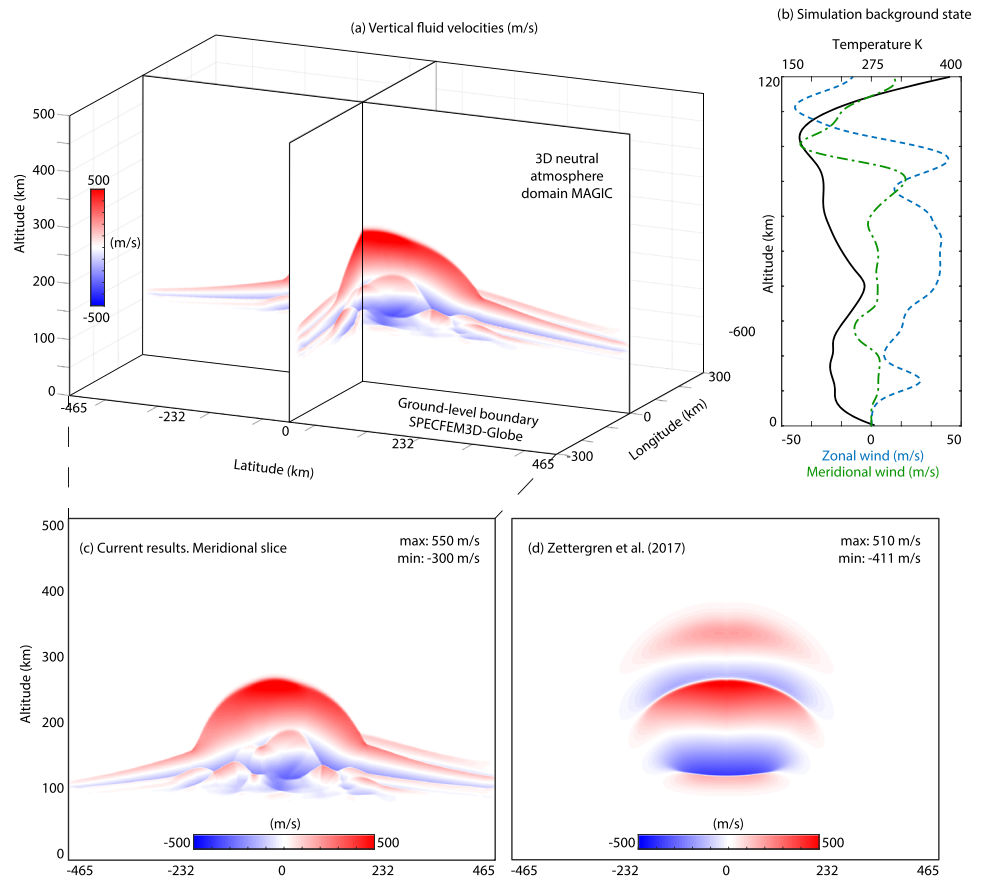


**Figure 1.** (a) Model configuration used for the simulation. The results of vertical fluid velocity are shown on the slide at  $T = 540$  s from rupture nucleation using cross-section slices. (b) Background temperature and wind profiles used in simulation. Comparison of vertical fluid velocities in their maxima at the altitude of  $\sim 270$  km from (c) current simulation and (d) Zettergren et al. (2017) (refer to section 4).

## 2. Modeling Approach and Assumptions

Our modeling approach is based on the coupling of temporally and spatially realistic surface displacements (driven by the earthquake) with the 3D MAGIC model (Figure 1a). Surface displacements were simulated with the SPEC-FEM3D\_GLOBE 3D forward seismic wave propagation model (Komatitsch & Tromp, 2002b; Komatitsch et al., 2009) and then used to drive MAGIC at its bottom boundary, which represents the Earth's surface. MAGIC solves numerically the compressible, nonlinear Navier-Stokes equations using a shock-capturing finite-volume scheme (Snively, 2013), based on the methods from Langseth and LeVeque (2000) and Bale et al. (2002) in a modified version of Clawpack 4.2 (Clawpack Development Team, 2002; LeVeque, 2002). It simulates AGW dynamics in neutral atmospheres and includes mesospheric airglow chemistry (Snively et al., 2010; Snively, 2013; Zettergren & Snively, 2015).

The offshore component of the earthquake source generates compressional hydro-acoustic and tsunami waves, and both may result in a sea-surface height change. In our simulation, we consider atmospheric dynamics driven by seismic waves of periods longer than 23 s. Also, the wavelengths  $\lambda$  of Rayleigh waves (RW—a seismic surface wave causing the ground to shake in an elliptical motion), resolved in our simulation, are not shorter than  $\sim 70$ – $80$  km and the ocean depth  $H$  is 1–5 km in the region considered ([www.maps.ngdc.noaa.gov/viewers/wcs-client/](http://www.maps.ngdc.noaa.gov/viewers/wcs-client/)). Ocean AWs are longitudinal waves with periods of usually lower than  $\sim 10$  s (Nosov et al., 2015) with sets of horizontally propagating modes. In the case of  $\lambda \gg H$ , seismic wave dynamics at the bottom result in practically equivalent vibrational motion of the ocean surface (Levin & Nosov, 2016; Saito, 2019). For  $\lambda \ll H$ , the solid-liquid interface supports Scholte mode (Kessel, 1996); otherwise, surface waves generated at the crust-water interface are RWs and behave as in the absence of the ocean (Kessel, 1996; Kennett, 2009).

In general, ocean compressibility has a negligible effect on the initial tsunami distribution, and it is a usual approach to consider the ocean surface height change to mimic the displacements at the ocean bottom (Kozdon & Dunham, 2014; Lotto & Dunham, 2015; Satake, 1987). This is particularly true for large size and long duration sources, as in the case of the 2011 Tohoku-Oki earthquake (Lay, 2018). Thus, in the simulation, we assume that permanent and transient (driven by seismic waves with periods  $>23$  s) ocean bottom displacements result in the same instantaneous sea-surface height change and use them directly as a source of AGWs in the atmosphere in the MAGIC model without considering dynamics within the ocean. This relaxes the need for detailed modeling of ocean responses to the undersea earthquake but may not be appropriate in case of the incorporation of high-frequency content of seismic waves, rapid faulting processes, or small fault sizes (Kajiura, 1963; Saito & Furumura, 2009). Also, we do not simulate the propagation of the tsunami and related atmospheric dynamics, concentrating our attention on MA responses to infrasonic AWs driven by vertical displacements. Vertical group velocities of internal atmospheric gravity waves generated by tsunamis are  $\sim 50$  m/s (Ochipinti et al., 2011). This is substantially slower than the speed of sound in the atmosphere ( $\sim 280$ – $340$  m/s in the considered region). Tsunamigenic gravity waves reach MA altitudes  $\sim 25$ – $30$  min after the earthquake and thus are not considered in our simulation of atmospheric dynamics during 12.5 min after rupture nucleation. The atmospheric and ionospheric responses to tsunami-driven gravity waves are intended to be investigated separately in a complementary study.

Extensive observations from regional and global seismic, geodetic, and ocean instrumentation networks provide a unique opportunity for the investigation of earthquake faulting mechanisms. However, the complexity and variety of models, based on different algorithms, datasets, and assumptions, make it challenging to select a single source representation that comprehensively explains all phenomena of interest (Lay, 2018). After reviewing available kinematic slip models, we have chosen one by Shao et al. (2011) (Model III), which is found to be appropriate for forward seismic wave propagation simulation, as well as for tsunami simulation (MacInnes et al., 2013; Ren et al., 2013). Source inversion results show satisfying agreement with near-field final displacements, based on GPS measurements and tsunami observations.

The 3D forward seismic wave propagation simulation is resolved up to  $\sim 0.043$  Hz. S362ANI, and CRUST2.0 Earth interior models are used (Bassin et al., 2000; Kustowski et al., 2008). Ocean and gravity effects are incorporated, as discussed in Komatitsch and Tromp (2002a). The MAGIC simulation is resolved with a uniform 500-m resolution for the domain  $1,200 \times 1,200 \times 200$  km in meridional, zonal, and vertical directions, respectively (note that 250-m resolution test cases found equivalent results, albeit at very high cost, confirming reasonable convergence). Top and side boundaries of the MAGIC numerical domain are effectively open. At the bottom boundary, we initially impose vertical velocities (calculated with SPEC3D\_GLOBE) and enforce a closed boundary condition after 415 s to incorporate possible AW reflections at the surface. Meridional and zonal winds, as well as temperature profiles for altitudes up to 55 km, were used from the MERRA-2 database. For higher altitudes, empirical models NRLMSISE00 (Picone et al., 2002) and HWM-14 (Drob et al., 2015) were used (Figure 1b). MERRA-2 data are selected for 15:00:00 LT, 14 min after rupture initiation. The background profiles remain stationary, and their change is found to be insignificant for the short simulation time frame across the spatial domain. The calculation of photochemistry for OH(3,1) and O(<sup>1</sup>S) modeling is based on the approach reported in Snively et al. (2010) using the chemistry of Adler-Golden (1997) and Makhlof et al. (1995, 1998). As we investigate only relative perturbations of the emitting layers, the results are less sensitive to the specific rate coefficients used. The earthquake occurred during comparatively active geomagnetic time (Dst index  $\sim -61$  nT). We did not include the topography/bathymetry to SPEC3D\_GLOBE simulation, because their effect on long-period seismic wave propagation is fairly small. For the details of the modeling process, we also refer to Inchin et al. (2020) that is devoted to the 2015 Nepal M7.8 earthquake case study and based on a similar modeling approach.

### 3. Model Simulation Results

For validation purposes, we compare our results with simulations reported by Zettergren et al. (2017) and Zettergren and Snively (2019). They investigated ionospheric responses to AGWs excited near the epicenter and found good agreement of simulation results with TEC observations, as well as confirming the formation of an ionospheric depletion. We compare neutral vertical fluid velocities at altitudes of  $\sim 270$  km (see Figures 1c and 1d) and find good agreement between our 3D and their original 2D axisymmetric simulations. Our simulation provides more comprehensive dynamics of AWs driven by the offset near the epicenter, and AWs driven by transient displacements at further distances from seismic wave propagation.



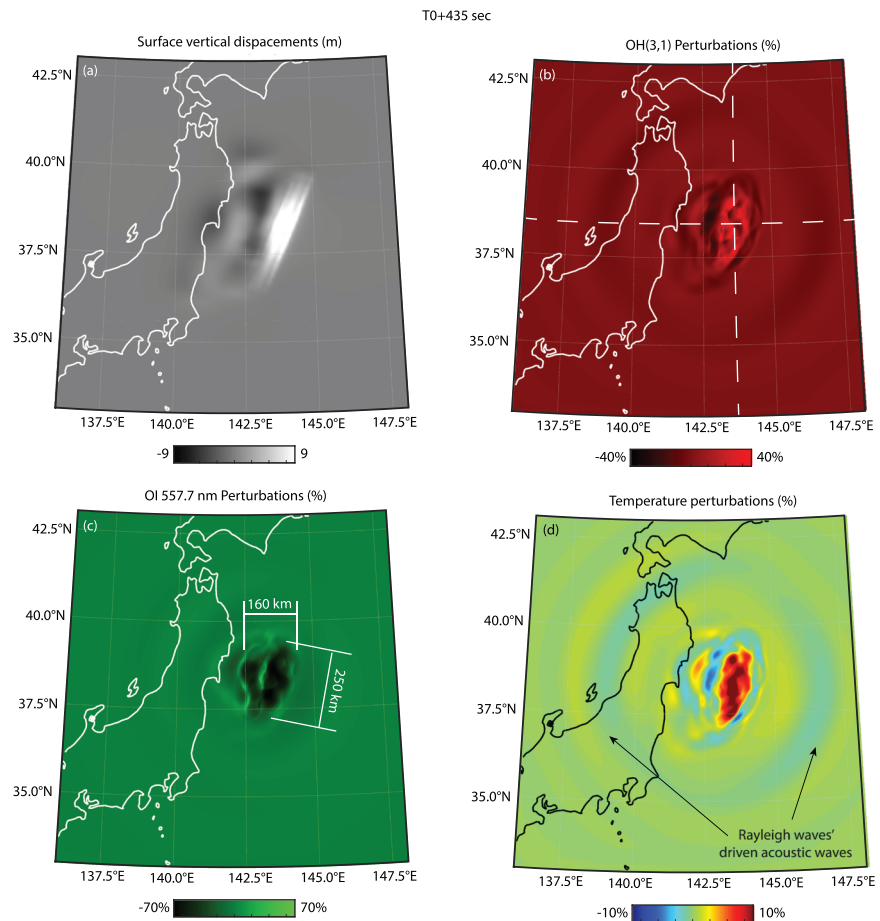


**Figure 2.** (a) Map of final vertical displacements. Vertically integrated (b) OH(3,1) and (c) O(<sup>1</sup>S) photon volume emission rate and (d) OH(3,1) BWT perturbations 435 s after rupture nucleation. Dashed lines represent meridional and zonal slices used for keograms. The movie, as well as data for 3D OH(3,1) and O(<sup>1</sup>S) volume emission rates, can be found in the supporting information.

Simulated perturbations of vertically integrated airglow OH(3,1) and O(<sup>1</sup>S) emission rates and OH(3,1) brightness-weighted temperature (BWT), which are calculated as discussed in section 3.1.3 in Snively et al. (2010) and represent the simplified observational geometry of ground-based imagers, are presented in Figure 2. The snapshots correspond to the time 435 s after Tohoku-Oki earthquake rupture nucleation (defined by kinematic slip model at  $T_0=14:46:23$  LT). The map of final displacements is provided for reference in Figure 2a. Surface displacement dynamics developed to the east from the approximate JMA epicenter position and resulted in a maximum uplift of  $\sim 13$  m and subsidence of  $\sim 5$  m near the Japan Trench ( $\sim 38^\circ\text{N}/143.3^\circ\text{E}$ ). The final displacements obtained in our simulation are comparable with results based on other finite-source rupture models (MacInnes et al., 2013). The details of the kinematic slip model and rupture dynamics can be found in Shao et al. (2011). Simulation results show that AWs at altitudes of 87 and 95 km (at the peaks of the OH(3,1) and O(<sup>1</sup>S) layers), excited from near-epicentral displacements, may exhibit vertical fluid velocities from  $-200$  to  $120$  m/s and from  $-260$  to  $160$  m/s, respectively. Major gas temperature perturbations reach values from  $-50$  to  $35\text{K}$  at altitude 87 km and from  $-100$  to  $60\text{K}$  at 95 km. This points to stronger perturbations in the O(<sup>1</sup>S) layer ( $\sim 95$  km), due to its higher altitude, in comparison with perturbations in the OH(3,1) layer ( $\sim 87$  km). Amplitudes of vertical fluid velocities of AWs driven by RW at mesopause altitudes are in the range  $-40$  to  $30$  m/s and also exhibit nonlinear effects, although to a much lesser extent.

The perturbations in OH(3,1) emission rate and temperature appear at  $T_0+300$  s and at  $T_0+340$  s for O(<sup>1</sup>S) integrated emission rates. Perturbations (the departure from the initial state) peak at  $\sim 50\%$  and

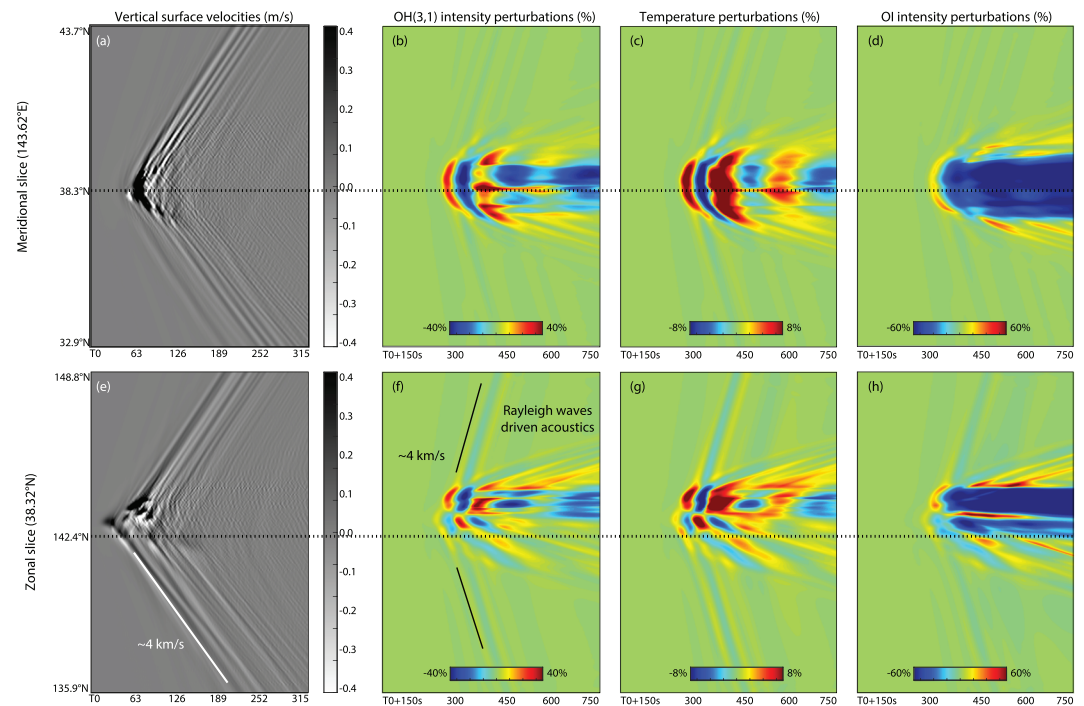


**Figure 3.** (a–d) Time–latitude diagrams of simulated vertical surface velocities (a), integrated OH(3,1) (b) and O(<sup>1</sup>S) (d) emissions, and temperature (c) perturbations along the longitude of approximately highest vertical surface displacements 143.67°E. (e–h) Time–longitude diagrams of the same perturbations as on panels (a)–(d) but along the latitude 38.32°N.  $T_0$  represents time of rupture nucleation. Plot color scales are oversaturated for better visibility.

~70% in OH(3,1) and O(<sup>1</sup>S) emission rates, respectively. OH(3,1) emission rate perturbations appear earlier due to the fact that the OH(3,1) layer is situated at lower altitudes than O(<sup>1</sup>S) (see Figure 4). OH(3,1) brightness-weighted temperature perturbations peak at ~15% and reach values  $-25/+37$ K. The propagation of AWs is followed by the decrease in OH(3,1) and O(<sup>1</sup>S) emission rates that is persistent over multiple oscillations from the propagation of AWs and concluded by a comparatively long-period recovery phase (depletion). The spatial extent of the depletion is  $\sim 160 \times 250$  km and resembles the shape, orientation, and size of the region of largest seafloor displacements. Our simulation shows perturbations of 1–5% in OH(3,1) and O(<sup>1</sup>S) integrated volume emission rates driven by RW AWs.

Time evolutions of simulated surface vertical velocities, OH(3,1), O(<sup>1</sup>S) integrated emission rates, and brightness-weighted temperature are shown in Figure 3. MA layers exhibit strong perturbations, driven by AWs from near-field displacements. MA perturbations driven by RW-excited AWs are also visible in the simulations, even at distances 600 km from the epicenter, though much weaker. Apparent phase velocities of excited MA perturbations from RW AWs correspond to phase velocities of RWs at the ground and are  $\sim 4$  km/s. Note that seismic and atmospheric AWs of periods  $> 23$  s are resolved in the simulation, and, thus, airglow perturbations reveal responses to only low-frequency RWs, whereas higher frequency content of AWs excited by RWs may be still present at these altitudes. Though not clearly detectable on time evolution diagrams, there are also MA perturbations driven by AWs generated by body waves, but their amplitudes are negligible (likely undetectable), in comparison with near-field and RW' driven AWs. Whereas there is no marked depletion in OH(3,1) integrated emission rate, it can be clearly seen for O(<sup>1</sup>S) after the propagation of acoustic shock waves. This is due to their impacts on the oxygen layer and taking into account that AW amplitudes of velocities at altitudes of O(<sup>1</sup>S) emission layer are substantially higher than those at OH(3,1) layer, due to exponential decrease of atmospheric density with altitude (Bergmann, 1946).

Figures 4a to 4c show the series of snapshots of OH(3,1) and O(<sup>1</sup>S) volume emission rates for meridional slice along 143.62°E—the same as used in Figure 3. Calculated emission rates for both species are overlaid on the same plots. The perturbations in both emitting layers coincide with the dynamics of AW propagation. Leading AWs result in steep and substantial displacement of layers upward and outward (Figure 4a) and are particularly strong in the O(<sup>1</sup>S) layer. Further, nonlinear oscillations of MA follow the downward



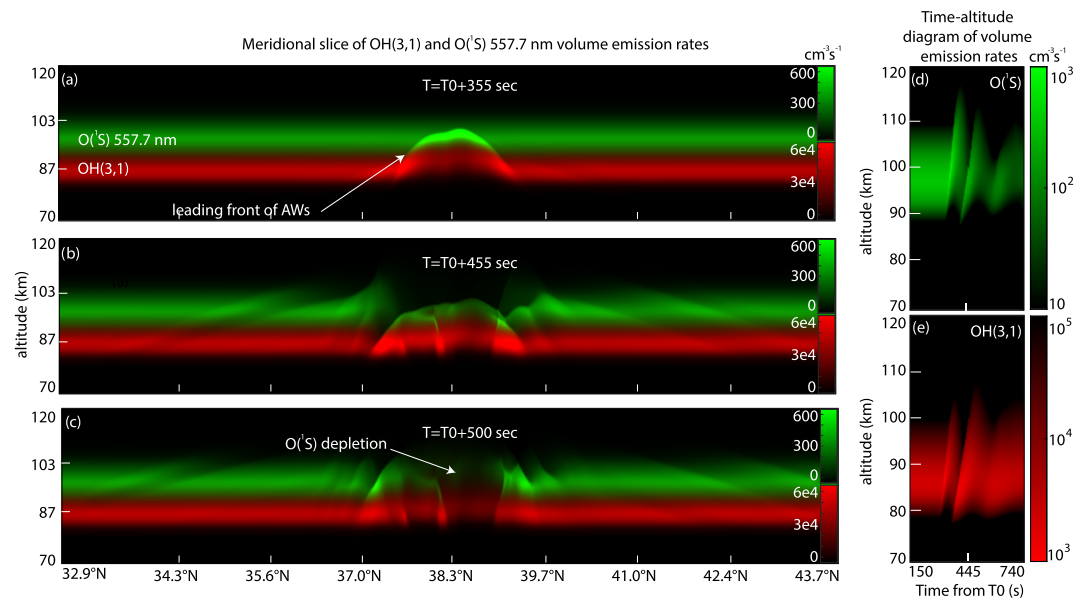


**Figure 4.** (a–c) Latitude–altitude diagrams of OH(3,1) and O(1S) volume emission rates at three moments of time. The plots are compressed horizontally to clearly represent perturbations. (d,e) OH(3,1) and O(1S) volume emission rates time–altitude diagrams. The movie, as well as data for meridional and zonal slices with altitude of OH(3,1) and O(1S) volume emission rates, can be found in the supporting information.

motion of the initial layers (Figure 4b) and by further upward displacements, etc. Figures 4d and 4e presents time–altitude diagrams for location 38.32°N/143.62°E. Partially, this depletion is driven by advection, leading to the displacements of minor species layers and reduced emission rates. At ~400 s after rupture nucleation, a substantial “hole” in O(1S) volume emission rate is detectable (see Figures 3d and 3h and Figure 4c), whereas OH(3,1) layer exhibits smaller depletion of the emission; these differences are largely explained by different amplitudes of AWs in each layer.

#### 4. Discussion

The results shown are based on the finite-fault model of Shao et al. (2011) (Model III); we also considered the kinematic slip model by Melgar and Bock (2015), which is based on near-field data and may provide better spatial and time control of the source. The results of MA perturbations based on this model are up to ~36% and ~70% in OH(3,1) and O(1S) integrated volume emission rates, respectively, and ~9% in OH(3,1) temperature. Though a bit weaker (but still comparable), the amplitudes of the perturbations based on this model support our main conclusion: The nonlinear AWs generated at the near-field region during large earthquakes can drive substantial perturbations in MA, which can potentially be observable with modern imagers. Modern MA imagers are sensitive to perturbations to both emissions considered here, for example, with sensitivity to 1% intensity and ~1 K temperature for hydroxyl (Pautet et al., 2014; Schmidt et al., 2013).

It should be noted that the fault model by (Melgar & Bock, 2015) cannot be adapted for forward seismic waves propagation simulation in SPECIFEM3D\_GLOBE without extensive new development. Thus, for this simulation, we considered only temporal and spatial offset dynamics without directly simulating seismic waves propagation that may results in lower amplitudes of AWs. The use of comparatively large subfaults in this model, which is appropriate for the main purpose of the original investigation of Melgar and Bock (2015) emphasizing tsunami formation, provides discontinuities at the edges of subfaults that drive surface deformations and subsequently AWs in atmosphere. Thus, the results of MA perturbations simulation based on the (Melgar & Bock, 2015) model are provided only in the supporting information materials to this manuscript for reference. Also, the wide range of peak vertical displacements reported based on different models (7–20 m, e.g., Lay, 2018) may lead to underestimation/overestimation of simulated MA responses that is not possible to validate; direct observations of offset or MA perturbations are needed to quantify precisely the amplitudes of AWs and perturbations in MA. This indicates needs and opportunities

for observational instrumentation deployments and further modeling studies, which may lead to important applications, for example, the estimation of ocean bottom displacements amplitudes based on MA observations.

Astafyeva and Heki (2009) and Occhipinti et al. (2018) reported that ionospheric observation, such as high-frequency Doppler, TEC, and radar measurements, can be a useful seismological data source. GNSS TEC represents the observations of plasma responses to AGWs roughly at the altitudes 250–300 km, where the coupling of neutral gas with plasma is effective. The amplitudes of AGWs, affected by strong dissipation at these altitudes and marked enhancement of nonlinear effects, should also be taken into account (Heale et al., 2014; Sabatini et al., 2019). In addition, because the plasma in the F-region of the ionosphere moves most easily along geomagnetic field lines and experiences ambient drift, its motion is not a direct representation of AW effects (e.g., Hooke, 1970; Nishioka et al., 2013; Zettergren & Snively, 2019); MA perturbations, driven by the neutral gas, do not suffer from this issue. For instance, for the analysis of RW propagation speeds, MA measurements may be used for the detection and analyses of RW AWs, which are not yet affected by strong dissipation at mesopause altitudes. Although detectable for the example shown, which represents a very large earthquake, it is important to note that the characteristics of RW AWs, and subsequently the presence of RW signatures, depend on the earthquake's magnitude and faulting mechanism, as well as on properties of the propagation media for the seismic waves (Udías et al., 2014). The investigation of spatial and temporal faulting dynamics, based on observations of MA perturbations, may also be possible for certain events, and these possibilities remain to be verified through detailed observational and/or modeling studies.

It is reasonable to assume that amplitudes of upper atmosphere responses are approximately correlated with amplitudes of ocean surface displacements (e.g., where initial tsunami disturbances provide a source of AWs in the atmosphere) and thus can be used for the characterization of the initial tsunami distribution. Recently, the possibility of early tsunami warning systems, based on TEC observations, have attracted considerable attention (Kamogawa et al., 2016; Occhipinti et al., 2013; Savastano et al., 2017). Our results suggest that MA observations may supplement such systems, particularly at nighttime. The Tohoku-Oki earthquake occurred in the vicinity of the Japanese coast (~70 km offshore), and wide field imagers (i.e., with fields of view of 120–180°) installed on the coast or even inland, as well as imagers aimed off-zenith over the ocean, could have readily detected the simulated MA perturbations arising from AWs excited by a nighttime equivalent of this earthquake. In order to demonstrate this, we synthesized images that can be obtained with such an airglow imager; the results are presented in Figure 5. The images of the integrated vertical emission rates (IVER) of OH(3,1) are created by integrating through the line-of-sight (LOS) of each  $512 \times 512$  pixel through the 3D OH(3,1) airglow layer volume emission rate data. An imager is first defined from its lens profile and field-of-view (FOV) and then rotated to be aligned with north or pointed at a desired tilt and azimuth angle, at any given surface height, latitude, or longitude. In this case, the imager is placed at the eastmost point along Japan's coast, roughly at the same latitude of the strongest perturbations in OH(3,1), and it is looking into zenith direction (Figure 5a) and at 40° tilt and eastward 90° azimuth (Figure 5b), which is pointing at the center of the data at 87-km height. The algorithm solves for the intersection of each pixel's LOS and an ellipsoid that represents an atmospheric thin layer at each height; this ellipsoid is determined by taking the ellipsoid that represents the surface of the Earth and expanding it by an ellipsoidal height that matches the vertical resolution. The LOS is set with 1-km resolution for every pixel (to capture scales of several kilometers), and this effectively maps a thick airglow layer on a 2D pixel surface, such as a CCD sensor. This is done for both perturbation and background data to obtain relative perturbations as shown in Figure 2. The resulting synthetic image is then unwarped at the mean peak OH(3,1) airglow height (87 km) by using the same LOS-ellipsoid intersection equations and subsequently plotted on a projected map (Figures 5c and 5d). An opacity of 67% has been added to the unwarped images to visualize the topography and bathymetry at ground level. The imager was placed at the location 38.3220°N/141.5219°E.

Simulation results suggest that substantial perturbations in MA would have been clearly imaged ~6 min after rupture initiation. First arrivals of tsunami to the shore of Japan were detected ~15–20 min after the earthquake (Mori et al., 2011). Thus, the time between possible detection of airglow perturbations, indicating ocean displacements, and tsunami arrival is sufficiently short to be useful for near-shore tsunami early-warning systems, in addition to other techniques and instrumentation. According to our simulation and observations reports, clear detection of perturbations in MA can be registered ~3 min earlier than in TEC for the Tohoku-Oki earthquake, 6 min and 9–10 min after the earthquake, respectively. The synthetic MA data also include AW features with smaller scales and shorter periods than those captured by TEC,

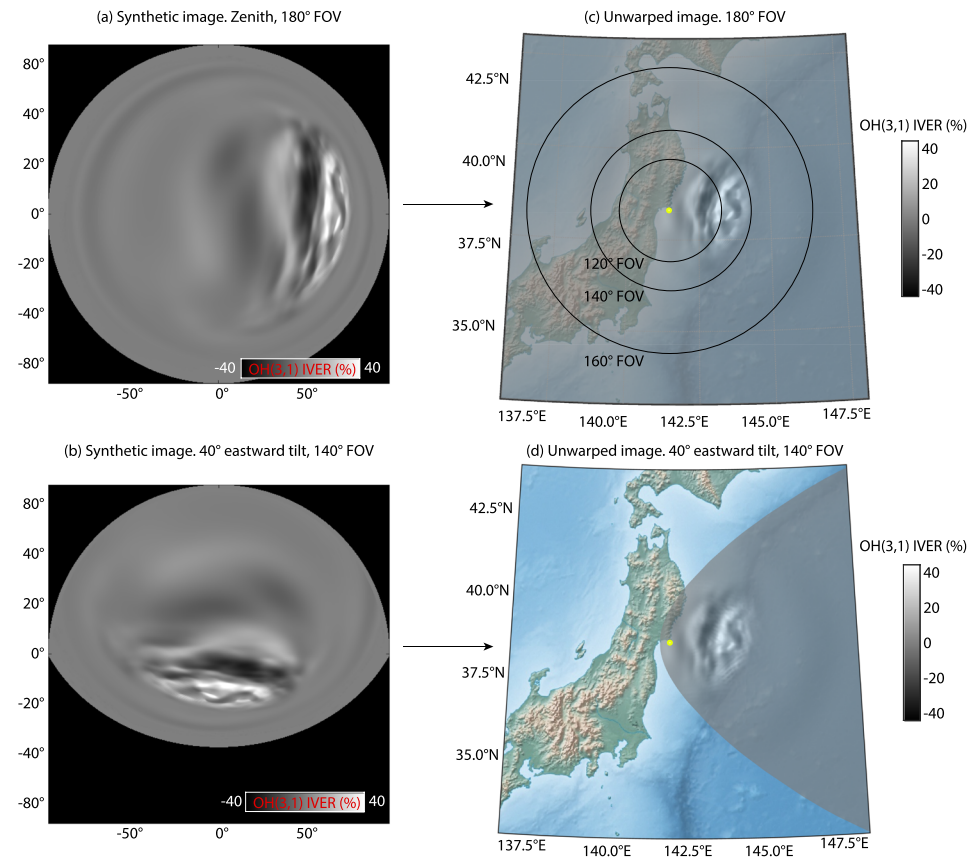


**Figure 5.** Synthetic images of OH(3,1) integrated volume emission rates (IVER) for (a) a zenith pointing wide field (180°) imager and (b) an eastward pointing imager with 40° tilt angle of 140° FOV. (c,d) Synthetic images unwrapped on a geographic map and shown on an oversaturated scale for better visibility of weaker features. Black circles in plot (c) show observable regions for imagers with 120°, 140°, and 160° FOVs, whereas a wide field imager covers the whole region. The yellow point in plots (c) and (d) represents the position of the imager.

potentially revealing more information about their source processes. Also, low electron density in the ionosphere during the night may result in fairly small (less detectable) TEC perturbations, even if AWs have marked amplitudes, whereas MA observations do not suffer from this problem and instead provide a complementary capability that favors nighttime detections. We want to note that the precise estimation of initial tsunami distribution may be complicated by the effective directivity of the AWs radiated by the source, as well as their interference, nonlinear evolution, and dissipation. In addition, strike-slip earthquakes with comparatively small vertical surface displacements may also result in upper atmosphere perturbations comparable in amplitudes with tsunamigenic earthquakes (with large vertical surface displacements), as it was demonstrated based on TEC observations by Astafyeva et al. (2014), and this requires further investigation.

## 5. Conclusions

Simulation results reported here demonstrate that AWs following large earthquakes (e.g., comparable to the Tohoku-Oki earthquake) are sufficiently intense to drive large perturbations in the OH(3,1) and O(<sup>1</sup>S) mesospheric nighttime airglow emissions. The airglow signatures of the nonlinear AWs would have been readily measurable from ground or space by contemporary imagers. The case reported here can be considered a nighttime analog to the 2011 Tohoku-Oki earthquake; airglow data may be able to provide actionable information, if measured, with strong shock responses confirming the presence of a very large ocean surface displacement as early as ~6 min following a similar type of event. New targeted observations above regions at high risk of seismic hazards may thus provide an additional source of data for tsunami early-warning systems, as well as new diagnostics of surface displacements (including amplitude and horizontal spatial characteristics) for seismological studies.

Three types of coseismic MA perturbations are discussed in this report, and their temporal and spatial characteristics can provide guidance on which requirements airglow imagers must meet for successful detection. First, large-amplitude MA perturbations, up to 50% and 70% in OH(3,1) and O(<sup>1</sup>S) IVER and up to 15% in OH(3,1) BWT, are generated over the focal area. Their sources are strongly nonlinear shock waves that exhibit dominant periods of ~60 s and vertical wavelengths of 17 km at mesopause altitudes. Second, a quasi-permanent depletion in VER, that is particularly strong in O(<sup>1</sup>S), can be observed over the focal area. As it was mentioned, the duration of MA depletion recovery depends on large-scale atmospheric dynamics that are not included into the simulation. However, as large-scale gravity and planetary waves act on much longer time intervals and periods, we speculate that MA depletion can be detected for at least several minutes, for example, a significant fraction of a buoyancy period, after the arrival of shock waves to mesopause altitudes, as simulated here. The area of MA perturbations and the depleted region is ~160 × 250 km with a center located ~70 km east of the coast of Japan. Finally, MA perturbations of 1–5% in OH(3,1) and O(1S) IVER and periods of ~50 s are driven by RW AWs and propagate with apparent horizontal phase velocities of ~4 km/s. Their small amplitudes and rapid passage through the field of view suggests that they could only be observed under optimal conditions and with special observing systems. In addition, RW AW wavefronts have low elevation angles (~20–25°), and their registration (as in the case of RW AWs observations in TEC) requires appropriate LOS directionality (Inchin et al., 2020). As the 2011 Tohoku-Oki earthquake was one of the strongest earthquakes in recent times, we also caution the reader that the characteristics of signals described above are applicable only to this or similarly scaled events.

It should be noted that the observations simulated here are most readily collected at night and the chemical systems used in modeling assume nighttime conditions. However, the primary results shown may have relevance beyond the specific chemical systems and emissions shown here. Indeed, the strength of the simulated AWs (which arrive as shocks for earthquakes of this scale and intensity) implies *very large dynamical perturbations to all measurable species layers throughout the mesopause region* (e.g., other emissions, metal species, or the ionospheric D-region; Marshall & Snively, 2014). The results suggest considerable opportunities for quantitative diagnostics of strong AWs passing through the mesopause, via active or passive optical or radio means.

Future works will be directed to the investigation of the correlation between MA responses, including OH(3,1) and O(<sup>1</sup>S) depletion formation and amplitudes of AWs based on simplified models and parametric studies in 1D and 2D. Currently, we also have deferred diagnosing the duration of the MA depletion's recovery, which requires the incorporation of realistic atmospheric dynamics driven by planetary, tidal, and gravity waves, ambient turbulence, and varying atmospheric states and winds, as well as more comprehensive chemistry. The knowledge of the neutral particle concentrations and their energetic coupling (e.g., Kalogerakis et al., 2018) in the mesosphere and lower thermosphere is also an important factor in deriving OH(3,1) and O(<sup>1</sup>S) production rates and subsequently the amplitudes of MA perturbations. The assumptions of the initial composition are also important; the ambient profile of atomic oxygen is used from NRLMSISE00 model, whereas some of the recent observational campaigns showed that NRLMSISE00 may underestimate densities of atomic oxygen (Mlynczak et al., 2013; Sheese et al., 2011).

To the best of our knowledge, this report presents the first simulations of MA emission perturbations driven by nonlinear AW shocks generated at the near-field region of an earthquake. Results support the hypotheses of Bittner et al. (2010) as to the potential value of airglow data for sensing hazard-generated AWs and also demonstrate the importance of nonlinearity, where signatures may persist following the passage of initial AWs. No equivalent airglow data for such events have been reported to date, and we are not aware of any data sets that would have captured the nonlinear phenomena predicted here for prior earthquakes. Thus, more detailed investigations, including model simulations of case studies based on prior earthquakes, as well as new airglow observations in seismically active regions, are needed. We will report other hypothetical case studies separately, in conjunction with analyses of ionospheric responses. Indeed, similar (observable) signatures are anticipated for weaker earthquakes, too, especially when large vertical displacements occur, but these signals may be too close to the detection threshold.

## References

- Adler-Golden, S. (1997). Kinetic parameters for OH nightglow modeling consistent with recent laboratory measurements. *Journal of Geophysical Research*, 102(A9), 19,969–19,976. <https://doi.org/10.1029/97JA01622>

### Acknowledgments

The finite-fault model used for forward seismic wave propagation simulation was taken from [https://ji.faculty.geol.ucsb.edu/big\\_earthquakes/2011/03/0311\\_v3/Honshu.html](https://ji.faculty.geol.ucsb.edu/big_earthquakes/2011/03/0311_v3/Honshu.html). Data characterizing the seismic source from Melgar and Bock (2015) and their availability are outlined in their respective references cited here. Dst index value was obtained from OMNIWEB system <https://omniweb.gsfc.nasa.gov/form/dx1.html>. Supporting information (animations and data) is also archived at the Embry-Riddle Aeronautical University Library Scholarly Commons, which can be found here: <https://commons.erau.edu/dm-mesopause-airglow-disturbances/>. This research was supported by NASA Grant NNX14AQ39G, 80NSSC18K1037, and 80NSSC20K0495 to ERAU and NSF CAREER Grants AGS-1255181 and AGS-1151746. The authors gratefully acknowledge the use of the ERAU Vega High-Performance Computing Cluster and the assistance of Scott Hicks. We also thank R. Sabatini for helpful discussions. Finally, we thank the reviewers, particularly Carsten Schmidt, for their helpful comments and suggestions.



- Astafeyeva, E., & Heki, K. (2009). Dependence of waveform of near-field coseismic ionospheric disturbances on focal mechanisms. *Earth, Planets and Space*, 61(7), 939–943. <https://doi.org/10.1186/BF03353206>
- Astafeyeva, E., Rolland, L. M., & Sladen, A. (2014). Strike-slip earthquakes can also be detected in the ionosphere. *Earth and Planetary Science Letters*, 405, 180–193. <https://doi.org/10.1016/j.epsl.2014.08.024>
- Azeem, I., Vadas, S. L., Crowley, G., & Makela, J. J. (2017). Traveling ionospheric disturbances over the United States induced by gravity waves from the 2011 Tohoku tsunami and comparison with gravity wave dissipative theory. *Journal of Geophysical Research: Space Physics*, 122, 3430–3447. <https://doi.org/10.1002/2016JA023659>
- Bale, D., LeVeque, R. J., Mitran, S., & Rossmanith, J. A. (2002). A wave-propagation method for conservation laws and balance laws with spatially varying flux functions. *SIAM Journal of Scientific Computing*, 24, 955–978. <https://doi.org/10.1137/S106482750139738X>
- Bassin, C., Laske, G., & Masters, G. (2000). The current limits of resolution for surface wave tomography in North America. *Eos Transaction AGU*, 81(F897), 7874–7880.
- Bergmann, P. G. (1946). The wave equation in a medium with a variable index of refraction. *The Journal of the Acoustical Society of America*, 17(4), 329–333. <https://doi.org/10.1121/1.1916333>
- Bittner, M., Hoepfner, K., Pilger, C., Schmidt, C., & Meyer-Arne, J. (2010). Infrasonic induced mesopause temperature perturbations as an early indicator for the detection of tsunamis and other geo-hazards. *Natural Hazards and Earth System Sciences*, 10, 1431–1442. <https://doi.org/10.5194/nhess-10-1431-2010>
- Blanc, E. (1985). Observations in the upper atmosphere of infrasonic waves from natural or artificial sources—A summary. *Annales Geophysicae*, 3, 673–687.
- Bolt, B. A. (1964). Seismic air waves from the Great 1964 Alaskan Earthquake. *Nature*, 202(4937), 1095–1096. <https://doi.org/10.1038/2021095a0>
- Clawpack Development Team (2002). Clawpack software. [http://www.clawpack.org,\\_Version4.2](http://www.clawpack.org,_Version4.2)
- Coisson, P., Lognonnè, P., Walwer, D., & Rolland, L. M. (2015). First tsunami gravity wave detection in ionospheric radio occultation data. *Earth and Space Science*, 2(5), 125–133. <https://doi.org/10.1002/2014EA000054>
- Drob, D. P., Emmert, J. T., Meriwether, J. W., Makela, J. J., Doornbos, E., Conde, M., et al. (2015). An update to the Horizontal Wind Model (HWM): The quiet time thermosphere. *Earth and Space Science*, 2(7), 301–319. <https://doi.org/10.1002/2014EA000089>
- Galvan, D. A., Komjathy, A., Hickey, M. P., Stephens, P., Snively, J., Tony Song, Y., et al. (2012). Ionospheric signatures of Tohoku-Oki tsunami of March 11, 2011: Model comparisons near the epicenter. *Radio Science*, 47, RS4003. <https://doi.org/10.1029/2012RS005023>
- Heale, C. J., Snively, J. B., Hickey, M. P., & Ali, C. J. (2014). Thermospheric dissipation of upward propagating gravity wave packets. *Journal of Geophysical Research: Space Physics*, 119, 3857–3872. <https://doi.org/10.1002/2013JA019387>
- Hooke, W. H. (1970). The ionospheric response to internal gravity waves: 1. The F2 region response. *Journal of Geophysical Research*, 75(28), 5535–5544. <https://doi.org/10.1029/JA075i028p05535>
- Inchin, P. A., Snively, J. B., Zettergren, M. D., Komjathy, A., Verkhoglyadova, O. P., & Tulasi Ram, S. (2020). Modeling of ionospheric responses to atmospheric acoustic and gravity waves driven by the 2015 Nepal Mw7.8 Gorkha earthquake. *Journal of Geophysical Research: Space Physics*, 125, e2019JA027200. <https://doi.org/10.1029/2019JA027200>
- Jin, S., Occhipinti, G., & Jin, R. (2015). GNSS ionospheric seismology: Recent observation evidences and characteristics. *Earth-Science Reviews*, 147, 54–64. <https://doi.org/10.1016/j.earscirev.2015.05.003>
- Kajitara, K. (1963). The leading wave of a tsunami. *Bulletin Earthquake Research Institute University Tokyo*, 41, 545–571.
- Kalogerakis, K. S., Matsiev, D., Cosby, P. C., Dodd, J. A., Falcinelli, S., Hedin, J., et al. (2018). New insights for mesospheric OH: Multi-quantum vibrational relaxation as a driver for non-local thermodynamic equilibrium. *Annales geophysicae*, 36, 13.
- Kamogawa, M., Orihara, Y., Tsurudome, C., Tomida, Y., Kanaya, T., Ikeda, D., et al. (2016). A possible space-based tsunami early warning system using observations of the tsunami ionospheric hole. *Nature Scientific Report*, 6, 37989. <https://doi.org/10.1038/srep37989>
- Kennett, B. (2009). *Seismic wave propagation in stratified media*. ANU Press, ISBN-10: 1921536721, 298. <https://doi.org/10.22459/SWPSM.05.2009>
- Kessel, R. (1996). *Scattering of elastic waves in layered media: A boundary integral normal mode approach*, (doctoral dissertation). Greater Victoria, British Columbia, Canada: University of Victoria, [https://dspace.library.uvic.ca/bitstream/handle/1828/6333/Kessel\\_Ronald\\_PhD\\_1996.PDF](https://dspace.library.uvic.ca/bitstream/handle/1828/6333/Kessel_Ronald_PhD_1996.PDF)
- Komatitsch, D., Michéa, D., & Erlebacher, G. (2009). Porting a high-order finite-element earthquake modeling application to NVIDIA graphics cards using CUDA. *Journal Parallel Distribution Computers*, 69(5), 451–460. <https://doi.org/10.1016/j.jpdc.2009.01.006>
- Komatitsch, D., & Tromp, J. (2002a). Spectral-element simulations of global seismic wave propagation -II. Three-dimensional models, oceans, rotation and self-gravitation. *Geophysical Journal International*, 150(1), 303–318. <https://doi.org/10.1046/j.1365-246X.2002.01716.x>
- Komatitsch, D., & Tromp, J. (2002b). Spectral-element simulations of global seismic wave propagation—I. Validation. *Geophysical Journal International*, 149(2), 390–412. <https://doi.org/10.1046/j.1365-246X.2002.01653.x>
- Komjathy, A., Yang, Y.-M., Meng, X., Verkhoglyadova, O., Mannucci, A. J., & Langley, R. B. (2016). Review and perspectives: Understanding natural-hazards-generated ionospheric perturbations using GPS measurements and coupled modeling. *Radio Science*, 51(7), 951–961. <https://doi.org/10.1002/2015RS005910>
- Kozdon, J. E., & Dunham, E. M. (2014). Constraining shallow slip and tsunami excitation in megathrust ruptures using seismic and ocean acoustic waves recorded on ocean-bottom sensor networks. *Earth and Planetary Science Letters*, 396, 56–65. <https://doi.org/10.1016/j.epsl.2014.04.001>
- Kustowski, B., Ekström, G., & Dziewoski, A. M. (2008). Anisotropic shear-wave velocity structure of the Earth's mantle: A global model. *Journal of Geophysical Research*, 113, B06306. <https://doi.org/10.1029/2007JB005169>
- Langseth, J. O., & LeVeque, R. J. (2000). A wave propagation method for three-dimensional hyperbolic conservation laws. *Journal of Computational Physics*, 165(1), 126–166. <https://doi.org/10.1006/jcph.2000.6606>
- Lay, T. (2018). A review of the rupture characteristics of the 2011 Tohoku-oki Mw 9.1 earthquake. *Tectonophysics*, 733, 4–36. <https://doi.org/10.1016/j.tecto.2017.09.022>
- LeVeque, R. J. (2002). *Finite volume methods for hyperbolic problems*, Cambridge Texts in Applied Mathematics. Cambridge: Cambridge University Press.
- Levin, B. W., & Nosov, M. A. (2016). *General information on tsunami waves, seaquakes, and other catastrophic phenomena in the ocean*, Physics of tsunamis (pp. 1–34). Cham: Springer International Publishing.
- Liu, J.-Y., Chen, C.-H., Lin, C.-H., Tsai, H.-F., Chen, C.-H., & Kamogawa, M. (2011). Ionospheric disturbances triggered by the 11 March 2011 M9.0 Tohoku earthquake. *Journal of Geophysical Research*, 116, A06319. <https://doi.org/10.1029/2011JA016761>
- Lotto, G. C., & Dunham, E. M. (2015). High-order finite difference modeling of tsunami generation in a compressible ocean from offshore earthquakes. *Computational Geosciences*, 19(2), 327–340. <https://doi.org/10.1007/s10596-015-9472-0>

- MacInnes, B. T., Gusman, A. R., LeVeque, R. J., & Tanioka, Y. (2013). Comparison of earthquake source models for the 2011 Tohoku event using tsunami simulations and near-field observations. *Bulletin of the Seismological Society of America*, *103*(2B), 1256. <https://doi.org/10.1785/0120120121>
- Makela, J. J., Lognonn, P., Hbert, H., Gehrels, T., Rolland, L., Allgeyer, S., et al. (2011). Imaging and modeling the ionospheric airglow response over Hawaii to the tsunami generated by the Tohoku earthquake of 11 March 2011. *Geophysical Research Letters*, *38*, L00G02. <https://doi.org/10.1029/2011GL047860>
- Makhlouf, U. B., Picard, R. H., & Winick, J. R. (1995). Photochemical-dynamical modeling of the measured response of airglow to gravity waves: 1. Basic model for OH airglow. *Journal of Geophysical Research*, *100*(D6), 11,289–11,311. <https://doi.org/10.1029/94JD03327>
- Makhlouf, U. B., Picard, R. H., Winick, J. R., & Tuan, T. F. (1998). A model for the response of the atomic oxygen 557.7nm and the OH Meinel airglow to atmospheric gravity waves in a realistic atmosphere. *Journal of Geophysical Research*, *103*(D6), 6261–6269. <https://doi.org/10.1029/97JD03082>
- Marshall, R. A., & Snively, J. B. (2014). Very low frequency subionospheric remote sensing of thunderstorm-driven acoustic waves in the lower ionosphere. *Journal of Geophysical Research: Atmospheres*, *119*, 5037–5045. <https://doi.org/10.1002/2014JD021594>
- Maryama, T., & Shinagawa, H. (2014). Infrasonic sounds excited by seismic waves of the 2011 Tohoku-oki earthquake as visualized in ionograms. *Journal of Geophysical Research: Space Physics*, *119*, 4094–4108. <https://doi.org/10.1002/2013JA019707>
- Matsumura, M., Saito, A., Iyemori, T., Shinagawa, H., Tsugawa, T., Otsuka, Y., et al. (2011). Numerical simulations of atmospheric waves excited by the 2011 off the Pacific coast of Tohoku Earthquake. *Earth Planets Space*, *63*(7), 68. <https://doi.org/10.5047/eps.2011.07.015>
- Melgar, D., & Bock, Y. (2015). Kinematic earthquake source inversion and tsunami runup prediction with regional geophysical data. *Journal of Geophysical Research: Solid Earth*, *120*, 3324–3349. <https://doi.org/10.1002/2014JB011832>
- Meng, X., Verkhoglyadova, O. P., Komjathy, A., Savastano, G., & Mannucci, A. J. (2018). Physics-based modeling of earthquake-induced ionospheric disturbances. *Journal of Geophysical Research: Space Physics*, *123*, 8021–8038. <https://doi.org/10.1029/2018JA025253>
- Mlynczak, M. G., Hunt, L. A., Mast, J. C., Thomas Marshall, B., Russell III, J. M., Smith, A. K., et al. (2013). Atomic oxygen in the mesosphere and lower thermosphere derived from saber: Algorithm theoretical basis and measurement uncertainty. *Journal of Geophysical Research: Atmospheres*, *118*, 5724–5735. <https://doi.org/10.1002/jgrd.50401>
- Mori, N., Takahashi, T., Yasuda, T., & Yanagisawa, H. (2011). Survey of 2011 Tohoku earthquake tsunami inundation and run-up. *Geophysical Research Letters*, *38*, L00G14. <https://doi.org/10.1029/2011GL049210>
- Nishioka, M., Tsugawa, T., Kubota, M., & Ishii, M. (2013). Concentric waves and short-period oscillations observed in the ionosphere after the 2013 Moore EF5 tornado. *Geophysical Research Letters*, *40*, 5581–5586. <https://doi.org/10.1002/2013GL057963>
- Nosov, M. A., Sementsov, K. A., Kolesov, S. V., Matsumoto, H., & Levin, B. W. (2015). Recording of gravity waves formed in the ocean by surface seismic waves during the earthquake of March 11, 2011, off the coast of Japan. *Doklady Earth Sciences*, *461*(5), 408–413. <https://doi.org/10.1134/S1028334X15040121>
- Occhipinti, G., Aden-Antoniow, F., Bablet, A., Molinie, J.-P., & Farges, T. (2018). Surface waves magnitude estimation from ionospheric signature of Rayleigh waves measured by Doppler sounder and OTH radar. *Nature Scientific Report*, *8*(1555). <https://doi.org/10.1038/s41598-018-19305-1>
- Occhipinti, G., Coisson, P., Makela, J. J., Allgeyer, S., Kherani, A., Hebert, H., & Lognonné, P. (2011). Three-dimensional numerical modeling of tsunami-related internal gravity waves in the Hawaiian atmosphere. *Earth Planets Space*, *63*(7), 61. <https://doi.org/10.5047/eps.2011.06.051>
- Occhipinti, G., Rolland, L., Lognonné, P., & Watada, S. (2013). From Sumatra 2004 to Tohoku-Oki 2011: The systematic GPS detection of the ionospheric signature induced by tsunamigenic earthquakes. *Journal of Geophysical Research: Space Physics*, *118*, 3626–3636. <https://doi.org/10.1002/jgra.50322>
- Pautet, P.-D., Taylor, M. J., Pendleton, W. R., Zhao, Y., Yuan, T., Esplin, R., & McLain, D. (2014). Advanced mesospheric temperature mapper for high-latitude airglow studies. *Applied Optics*, *53*(26), 5934–5943. <https://doi.org/10.1364/AO.53.005934>
- Picone, J. M., Hedin, A. E., Drob, D. P., & Aikin, A. C. (2002). NRLMSISE-00 empirical model of the atmosphere: Statistical comparisons and scientific issues. *Journal of Geophysical Research*, *107*(A12), 1468. <https://doi.org/10.1029/2002JA009430>
- Pilger, C., & Bittner, M. (2009). Infrasound from tropospheric sources: Impact on mesopause temperature? *Journal of Atmospheric and Solar-Terrestrial Physics*, *71*(8), 816–822. <https://doi.org/10.1016/j.jastp.2009.03.008>
- Pilger, C., Schmidt, C., Streicher, F., Wüst, S., & Bittner, M. (2013). Airglow observations of orographic, volcanic and meteorological infrasound signatures. *Journal of Atmospheric and Solar-Terrestrial Physics*, *104*, 55–66. <https://doi.org/10.1016/j.jastp.2013.08.008>
- Ren, Z.-Y., Wang, B.-L., Fan, T.-T., & Liu, H. (2013). Numerical analysis of impacts of 2011 Japan Tohoku tsunami on China coast. *Journal of Hydrodynamics, Series B*, *25*(4), 580–590. [https://doi.org/10.1016/S1001-6058\(11\)60399-6](https://doi.org/10.1016/S1001-6058(11)60399-6)
- Sabatini, R., Marsden, O., Bailly, C., & Gainville, O. (2019). Three-dimensional direct numerical simulation of infrasound propagation in the Earth's atmosphere. *Journal of Fluid Mechanics*, *859*, 754–789. <https://doi.org/10.1017/jfm.2018.816>
- Saito, T. (2019). Tsunami generation, *Tsunami generation and propagation* (pp. 149–203). Tokyo: Springer Japan.
- Saito, T., & Furumura, T. (2009). Three-dimensional tsunami generation simulation due to sea-bottom deformation and its interpretation based on the linear theory. *Geophysical Journal International*, *178*(2), 877–888. <https://doi.org/10.1111/j.1365-246X.2009.04206.x>
- Saito, A., Tsugawa, T., Otsuka, Y., Nishioka, M., Iyemori, T., Matsumura, M., et al. (2011). Acoustic resonance and plasma depletion detected by GPS total electron content observation after the 2011 off the Pacific coast of Tohoku earthquake. *Earth, Planets and Space*, *63*(7), 64. <https://doi.org/10.5047/eps.2011.06.034>
- Satake, K. (1987). Inversion of tsunami waveforms for the estimation of a fault heterogeneity: method and numerical experiments. *Journal of Physics of the Earth*, *35*(3), 241–254. <https://doi.org/10.4294/jpe1952.35.241>
- Satake, K., Fujii, Y., Harada, T., & Namegaya, Y. (2013). Time and space distribution of coseismic slip of the 2011 Tohoku earthquake as inferred from tsunami waveform data. *Bulletin of the Seismological Society of America*, *103*(2B), 1473–1492. <https://doi.org/10.1785/0120120122>
- Savastano, G., Komjathy, A., Verkhoglyadova, O., Mazzoni, A., Crespi, M., Wei, Y., & Mannucci, A. J. (2017). Real-time detection of tsunami ionospheric disturbances with a stand-alone GNSS receiver: A preliminary feasibility demonstration. *Nature*, *7*, 46607. <https://doi.org/10.1038/srep46607>
- Schmidt, C., Höppner, K., & Bittner, M. (2013). A ground-based spectrometer equipped with an InGaAs array for routine observations of OH(3-1) rotational temperatures in the mesopause region. *Journal of Atmospheric and Solar-Terrestrial Physics*, *102*, 125–139. <https://doi.org/10.1016/j.jastp.2013.05.001>
- Shao, G., Li, X., Ji, C., & Maeda, T. (2011). Focal mechanism and slip history of the 2011 Mw 9.1 off the Pacific coast of Tohoku earthquake, constrained with teleseismic body and surface waves. *Earth, Planets and Space*, *63*(7), 559–564. <https://doi.org/10.5047/eps.2011.06.028>



- Sheese, P. E., McDade, I. C., Gattinger, R. L., & Llewellyn, E. J. (2011). Atomic oxygen densities retrieved from optical spectrograph and infrared imaging system observations of O<sub>2</sub> a-band airglow emission in the mesosphere and lower thermosphere. *Journal of Geophysical Research*, *116*, D01303. <https://doi.org/10.1029/2010JD014640>
- Shinagawa, H., Tsugawa, T., Matsumura, M., Iyemori, T., Saito, A., Maruyama, T., et al. (2013). Two-dimensional simulation of ionospheric variations in the vicinity of the epicenter of the Tohoku-oki earthquake on 11 March 2011. *Geophysical Research Letters*, *40*, 5009–5013. <https://doi.org/10.1002/2013GL057627>
- Smith, S. M., Martinis, C. R., Baumgardner, J., & Mendillo, M. (2015). All-sky imaging of transglobal thermospheric gravity waves generated by the March 2011 Tohoku Earthquake. *Journal of Geophysical Research: Space Physics*, *120*, 10,992–10,999. <https://doi.org/10.1002/2015JA021638>
- Snively, J. B. (2013). Mesospheric hydroxyl airglow signatures of acoustic and gravity waves generated by transient tropospheric forcing. *Geophysical Research Letters*, *40*, 4533–4537. <https://doi.org/10.1002/grl.50886>
- Snively, J. B., Pasko, V. P., & Taylor, M. J. (2010). OH and OI airglow layer modulation by ducted short-period gravity waves: Effects of trapping altitude. *Journal of Geophysical Research*, *115*, A11311. <https://doi.org/10.1029/2009JA015236>
- Tsugawa, T., Saito, A., Otsuka, Y., Nishioka, M., Maruyama, T., Kato, H., et al. (2011). Ionospheric disturbances detected by GPS total electron content observation after the 2011 off the Pacific coast of Tohoku Earthquake. *Earth, Planets and Space*, *63*(7), 66. <https://doi.org/10.5047/eps.2011.06.035>
- Udías, A., Madariaga, R., & Buforn, E. (2014). *Source mechanisms of earthquakes: Theory and practice*. Cambridge: Cambridge University Press.
- Yang, Y.-M., Verkhoglyadova, O., Mlynczak, M. G., Mannucci, A. J., Meng, X., Langley, R. B., & Hunt, L. A. (2017). Satellite-based observations of tsunami-induced mesosphere airglow perturbations. *Geophysical Research Letters*, *44*, 522–532. <https://doi.org/10.1002/2016GL070764>
- Zettergren, M. D., & Snively, J. B. (2015). Ionospheric response to infrasonic-acoustic waves generated by natural hazard events. *Journal of Geophysical Research: Space Physics*, *120*, 8002–8024. <https://doi.org/10.1002/2015JA021116>
- Zettergren, M. D., & Snively, J. B. (2019). Latitude and longitude dependence of ionospheric TEC and magnetic perturbations from infrasonic-acoustic waves generated by strong seismic events. *Geophysical Research Letters*, *46*, 1132–1140. <https://doi.org/10.1029/2018GL081569>
- Zettergren, M. D., Snively, J. B., Komjathy, A., & Verkhoglyadova, O. P. (2017). Nonlinear ionospheric responses to large-amplitude infrasonic-acoustic waves generated by undersea earthquakes. *Journal of Geophysical Research: Space Physics*, *122*, 2272–2291. <https://doi.org/10.1002/2016JA023159>